

Annual Review of Physical Chemistry

Bose–Einstein Condensation of Exciton–Polaritons in Organic Microcavities

Jonathan Keeling¹ and Stéphane Kéna-Cohen²

¹Scottish Universities Physics Alliance, School of Physics and Astronomy, University of St. Andrews, St. Andrews KY16 9SS, United Kingdom; email: jmjk@st-andrews.ac.uk

²Department of Engineering Physics, École Polytechnique de Montréal, Montréal H3T 1J4, Canada; email: stephane.kena-cohen@polymtl.ca

Annu. Rev. Phys. Chem. 2020. 71:435–59

First published as a Review in Advance on
March 3, 2020

The *Annual Review of Physical Chemistry* is online at
physchem.annualreviews.org

<https://doi.org/10.1146/annurev-physchem-010920-102509>

Copyright © 2020 by Annual Reviews.
All rights reserved

**ANNUAL
REVIEWS CONNECT**

www.annualreviews.org

- Download figures
- Navigate cited references
- Keyword search
- Explore related articles
- Share via email or social media

Keywords

light–matter interaction, organic microcavities, polariton condensation, polariton lasing, strong coupling

Abstract

Bose–Einstein condensation describes the macroscopic occupation of a single-particle mode: the condensate. This state can in principle be realized for any particles obeying Bose–Einstein statistics; this includes hybrid light–matter excitations known as polaritons. Some of the unique optoelectronic properties of organic molecules make them especially well suited for the realization of polariton condensates. Exciton–polaritons form in optical cavities when electronic excitations couple collectively to the optical mode supported by the cavity. These polaritons obey bosonic statistics at moderate densities, are stable at room temperature, and have been observed to form a condensed or lasing state. Understanding the optimal conditions for polariton condensation requires careful modeling of the complex photophysics of organic molecules. In this article, we introduce the basic physics of exciton–polaritons and condensation and review experiments demonstrating polariton condensation in molecular materials.

1. INTRODUCTION

Exciton-polaritons are part-matter, part-light quasiparticles (1, 2). They are formed when electronic excitations mix strongly with electromagnetic radiation—a regime known as strong matter-light coupling. In this case, the normal modes of the system are not separate light and matter excitations but instead become hybrids, with properties inherited from both their matter and light constituents. In a confined geometry, such as an optical microcavity, polaritons inherit the small effective mass of the confined photon. From their matter constituent, they inherit interactions. In the simplest approximation, polaritons thus behave as a gas of interacting bosonic quasiparticles with a small effective mass.

Bose–Einstein condensation (BEC) occurs when the de Broglie wavelength of a particle, $\lambda_{dB} \propto 1/\sqrt{mk_B T}$, where m is particle mass, exceeds the interparticle spacing—a regime known as quantum degeneracy. As such, the small polariton mass, in principle, allows for condensation of polaritons at high temperatures (3, 4). This temperature is given by $k_B T_{deg} \propto \hbar^2 n^{2/d}/m$ for a gas of particles with mass m and density n in d dimensions (5). Existence of a polariton condensate also requires that the exciton binding energy and matter-light coupling be larger than the temperature. Molecular materials are able to satisfy this criterion up to high temperatures, enabling room-temperature quantum degeneracy to be observed.

In molecular solids, delocalized excitations termed Frenkel excitons form from the hopping of electronic excitations between molecules, or between chromophores in polymers. This contrasts with Wannier–Mott excitons in inorganic materials—bound states of delocalized electrons and holes (3). Because Frenkel excitons have a larger oscillator strength and binding energy than Wannier excitons, they can be observed and studied at room temperature. Other differences between organic and inorganic materials include the presence of significant energetic and positional disorder, particularly in amorphous molecular materials or polymers, and the existence of high-energy vibrational modes that can couple strongly to the electronic state. In this review, we discuss how these affect the properties of organic polaritons and, specifically, polariton condensates based on molecular materials.

Several potential applications underpin the scientific interest in microcavity polaritons and organic polaritons in particular. The most investigated is the ability of polariton condensates to be used as low-threshold coherent light emitters. In inorganic semiconductor microcavities, there is substantial evidence showing that the threshold for polariton lasing is lower than that for conventional photon lasing in analogous structures (6). Another application is gain-dissipative optimization machines using polaritons, where a computational problem is encoded in the gain and loss landscape of many coupled condensates (7). There are also proposals to use lattices of polariton condensates for analog quantum computation to address problems in driven-dissipative environments (8). Several proposals for polaritonic logic also exist, which rely on the existence of a nonlinear interaction between polaritons (9), enabling polariton density to modulate the flow of polaritons. Organic materials are a promising venue for the exploration of some of these ideas because of their ability, in contrast to most inorganic semiconductors, to be used at room temperature. In addition, their processing and fabrication can be significantly simpler than inorganic microcavities. Finally, organic semiconductors also have unique potential for applications building on the ways in which strong matter-light coupling, and possibly the creation of a condensate, can modify the photophysics and chemistry of organic molecules (10–12).

While there has been a long history of both theory (13) and experiments (14–19) on molecular polaritons, recent interest and activity in condensation followed from the 2010 observation of polariton lasing (20) in microcavities containing anthracene single crystals (21). Inhomogeneous broadening in such organic crystals is notably lower than in the amorphous or polycrystalline thin films conventionally used for organic electronics. More recent work, however, has shown that if

the polariton splitting exceeds the disorder linewidth, lasing is still possible, as demonstrated in amorphous molecular films (22–27), organic polymers (28–30), and even proteins (31, 32).

Polariton condensation and lasing—terms that we use interchangeably in this review—refer to any transition to a coherent state in which a single mode is macroscopically occupied. Condensation is used by analogy to BEC, a thermal equilibrium phase of matter, which involves macroscopic occupation of the lowest-energy mode of a system. In a system of many identical quantum particles, the occupation of the single-particle modes is given by the Bose–Einstein distribution. For a low enough temperature at a fixed particle density (or high enough density at a fixed temperature), this distribution predicts that a nonvanishing fraction of particles all occupy the same, lowest-energy mode. In contrast, at high temperatures, the average fraction of particles in a mode vanishes in the thermodynamic limit—that is, particles are spread out over many modes. The macroscopic occupation of a single mode leads to enhanced coherence in both space and time (5).

Since any real mirror is imperfect, light will escape. This escaping light is in fact how the microcavity polariton density, phase, and momentum are detected. It does mean, however, that the condensate can never be in perfect thermal equilibrium; there is always a loss of polaritons. In a very good cavity, when polariton lifetime is longer than thermalization time, a description in terms of BEC is appropriate (33). To date, experiments with organic polaritons are far from this regime, and full thermalization does not occur.

This review focuses on polariton condensates in organic materials. The broader topic of excitons in organic solids has been discussed in a number of books (34–36), some including discussion of polaritons. There are many reviews of polariton condensation, including the comprehensive review by Carusotto & Ciuti (4). More recent reviews discuss polaritonic devices and the material platforms supporting these (6). A closely related topic is how strong matter-light coupling can modify the photophysics and chemistry of molecules. This is beyond the scope of this review (see, for example, 10–12).

The remainder of this review is arranged as follows. Section 2 provides an introduction to polaritons, and Section 3 to polariton condensation and lasing. Section 4 reviews the materials and experiments in which organic polariton condensation has been seen. In Section 5, we provide a short summary of theoretical models; further details are given in the **Supplemental Appendix**. We conclude with comments on future directions and open questions.

Supplemental Material >

2. INTRODUCTION TO MICROCAVITY POLARITONS

2.1. Strong Coupling Between Light and Matter

An optical cavity confines light by trapping it between mirrors and gives rise to discrete optical modes for which the field is concentrated inside the cavity. It can therefore increase the coupling between light and matter, ultimately leading to the regime of strong coupling, where new normal modes arise.

The term strong coupling refers to the case where the coupling between matter and light exceeds the linewidth, so that new normal modes and the anticrossing of energies can be seen. More precisely, for coupling strength g and matter and photon linewidths γ, κ (half widths at half maximum), one requires $g^2 > (\gamma^2 + \kappa^2)/2$ (37). A simple model of a single-photon mode coupled to a two-level system is the Jaynes–Cummings model:

$$H = \omega \hat{a}^\dagger \hat{a} + \epsilon \sigma^+ \sigma^- + g(\sigma^+ \hat{a} + \text{H.c.}) \quad 1.$$

The two-level system (e.g., a saturable molecular transition) with energy ϵ is described through Pauli matrices σ^\pm corresponding to raising or lowering transitions between the two states, such

that σ^+ creates an exciton. The last term in Equation 1 describes coherent coupling between excitons and photons. This coupling is distinct from the incoherent absorption or emission rate. The coupling in the Jaynes–Cummings model is instead coherent, meaning one has new eigenstates, superpositions of exciton and photon. As Equation 1 conserves n_{ex} , the number of photons plus excitons, the eigenstates at fixed $n_{\text{ex}} > 1$ can be found as the eigenvalues of a 2×2 matrix:

$$b_{n_{\text{ex}}} = n_{\text{ex}}\omega + \begin{pmatrix} \epsilon - \omega & g\sqrt{n_{\text{ex}}} \\ g\sqrt{n_{\text{ex}}} & 0 \end{pmatrix}, \quad E_{n_{\text{ex}}}^{\pm} = (n_{\text{ex}} - 1)\omega + \frac{1}{2} \left[\epsilon + \omega \pm \sqrt{(\epsilon - \omega)^2 + 4g^2 n_{\text{ex}}} \right]. \quad 2.$$

If $\epsilon = \omega$, these modes are the symmetric and antisymmetric superposition of exciton and photon, and the transition from the $n_{\text{ex}} = 0$ ground state to the first excited state is split by $2g$ —the vacuum Rabi splitting. This splitting can be directly measured from the absorption, reflection, or transmission spectrum of such a system.

The coupling, g , for a single molecule is typically small. As the field strength scales as $1/\sqrt{V}$ for mode volume V , one approach to increase g is to decrease V . Generally, V is limited by the wavelength of light, λ^3 ; however, for evanescent fields—for example, the plasmonic resonance in the gap between a gold nanoparticle and a metal film (38)— V can be smaller. An alternative approach to increase the Rabi splitting is coupling many particles to the same cavity mode. Consider the many-particle model, known as the Tavis–Cummings model:

$$H = \omega \hat{a}^\dagger \hat{a} + \sum_n \epsilon \sigma_n^+ \sigma_n^- + g(\sigma_n^+ \hat{a} + \text{H.c.}). \quad 3.$$

The eigenstates for $n_{\text{ex}} = 1$ have energies $E^{\pm} = \frac{1}{2}[\epsilon + \omega \pm \sqrt{(\epsilon - \omega)^2 + 4g^2 N}]$, showing the enhanced Rabi splitting $g \rightarrow g\sqrt{N}$. These collective modes are polaritons: superpositions of a photon and delocalized molecular excitation, $|\pm\rangle = (U_{\pm} \sum_n \sigma_n^+ + V_{\pm} \hat{a}^\dagger)|0\rangle$, where $|0\rangle$ is a vacuum state and U_{\pm}, V_{\pm} are coefficients normalized by $NU_{\pm}^2 + V_{\pm}^2 = 1$.

As the system of N molecules and one photon has $N + 1$ degrees of freedom, there must be $N - 1$ other modes in addition to the two polaritons. These modes, known as dark states, correspond to states $\sum_n U_n^{(m)} b_n^\dagger |0\rangle$, where $\sum_n U_n^{(m)} = 0$, normalized by $\sum_n |U_n^{(m)}|^2 = 1$. As these states are all degenerate with energy ϵ , many possible orthonormal bases exist; one possible basis is that of plane waves, $U_n^{(m)} = \exp(i2\pi mn/N)/\sqrt{N}$, with $m = 1 \dots N - 1$.

2.2. Microcavity Polaritons

A typical context for collective strong coupling consists of molecules in a planar microcavity (see **Figure 1**). The cavity length is chosen so at least one mode is close to resonance with the exciton. The size in the transverse direction is less important, as the N -fold coupling enhancement means the splitting depends on $\rho \equiv N/A$, the areal density of molecules.

We model this planar cavity with a generalized Tavis–Cummings model:

$$H = \sum_{\mathbf{k}} \omega_{\mathbf{k}} \hat{a}_{\mathbf{k}}^\dagger \hat{a}_{\mathbf{k}} + \sum_n \epsilon_n \sigma_n^+ \sigma_n^- + \sum_{n,\mathbf{k}} g(\sigma_n^+ \hat{a}_{\mathbf{k}} e^{i\mathbf{k}\cdot\mathbf{r}_n} + \text{H.c.}), \quad 4.$$

where the molecule-photon coupling has a phase factor depending on the in-plane wavevector \mathbf{k} and the molecular position \mathbf{r}_n . As shown in **Figure 1**, the cavity photon dispersion is modified from the free space form $\omega_{\mathbf{k}} = ck$ and becomes $\omega_{\mathbf{k}} = c\sqrt{\mathbf{k}^2 + (2\pi p/L)^2}$, where \mathbf{k} is the in-plane wavevector, p is an integer, and L is the effective cavity length. This dispersion is quadratic at low momentum, $\omega_{\mathbf{k}} \approx \omega_0 + \hbar^2 k^2 / 2m_{\text{ph}}$, where m_{ph} is the photon mass, which is typically 10^4 times smaller than the electron mass. For low excitation density, one can approximate the two-level system operators σ^+ ,

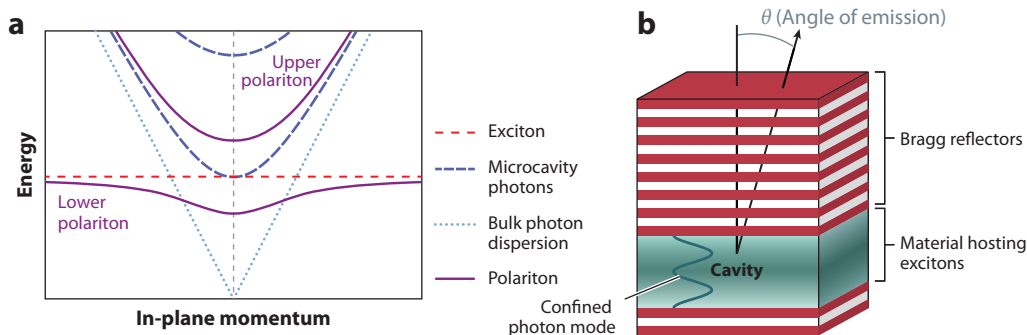


Figure 1

(a) Microcavity polariton spectrum (purple), resulting from hybridization between microcavity photons (blue) and excitons (red). The blue dotted line shows the bulk photon dispersion. (b) Diagram of a microcavity, with mirrors formed of distributed Bragg reflectors (alternating white and red layers) and material hosting excitons (green).

σ^- by bosonic operators \hat{b}^\dagger, \hat{b} and Fourier transform $\hat{b}_n = \sum_k \hat{b}_k e^{-ik \cdot r_n} / \sqrt{N}$ to find the polaritonic dispersion (see **Figure 1**):

$$E_k^\pm = \frac{1}{2} \left[\epsilon + \omega_k \pm \sqrt{(\omega_k - \epsilon)^2 + 4g^2 N} \right]. \quad 5.$$

The energy difference $\omega_{k=0} - \epsilon$ is referred to as the detuning of the cavity.

The cavity mirrors can be either metallic or dielectric. For metals, the physical cavity length corresponds approximately to the optical length (39). However, metal mirrors have relatively low reflectivities, <99%, which limits the cavity photon lifetime. For this reason, all polariton BEC experiments in planar microcavities use high-reflectivity dielectric mirrors. Such mirrors, known as distributed Bragg reflectors (DBRs), consist of alternating $\lambda/4$ -thick layers of high/low dielectric constant. One disadvantage of DBRs is that the large field penetration into the mirrors increases the effective cavity length (and hence the mode volume), which reduces the achievable Rabi splitting (40).

Not all polariton experiments involve planar microcavities; an increasing number of experiments use an open cavity design, involving a planar bottom mirror and a curved top mirror mounted on the end of an optical fiber (41). For such cavities, the photon spectrum consists of discrete levels due to the additional transverse confinement. Another open geometry that has demonstrated condensation involves the use of plasmon surface lattice resonances supported by the diffractive coupling between localized surface plasmon resonances in an array of metallic particles (42, 43).

2.3. Measuring the Polariton Dispersion Relation

For planar layers, electromagnetic boundary conditions dictate that the in-plane component of the wavevector be preserved on both sides of any interface. As a result, the in-plane component of the polariton wavevector matches the in-plane wavevector of the emitted light. The polariton dispersion relation can thus be measured directly via the photoluminescence, reflection, or transmission spectra of the microcavity versus the in-plane wavevector, or, equivalently, the angle θ with respect to the cavity normal, as illustrated in **Figure 1**. The in-plane wavevector relates to the angle of the emitted light via $k = k_0 \sin \theta = \frac{\omega_0}{c} \sin \theta$, where ω_0 is the photon angular frequency and k_0 is the norm of the total wavevector in free space. Resonances corresponding to

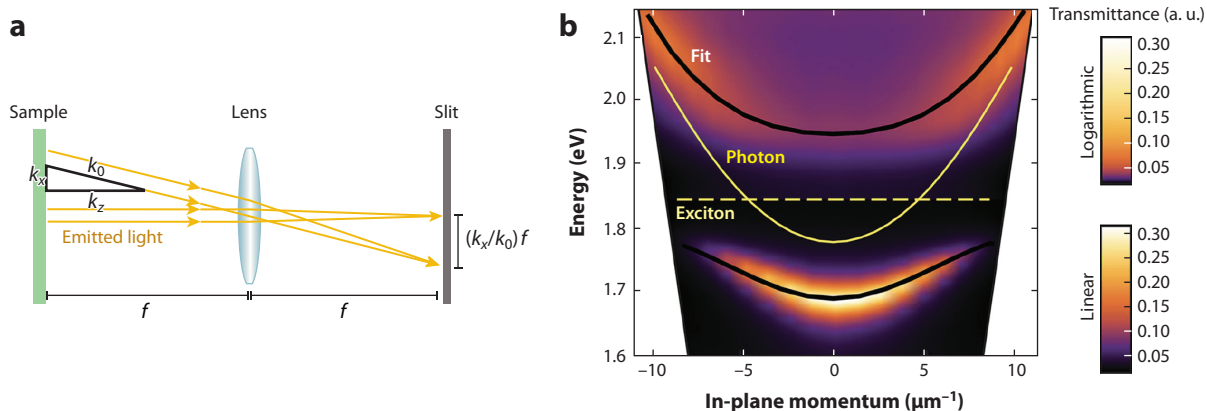


Figure 2

(a) Configuration for Fourier-space imaging. A lens (or microscope objective) with focal length f projects the Fourier components of the emitted light onto the entrance slit of a spectrometer placed f away. (b) Contour plot of the angle-resolved transmission from a microcavity containing a squaraine dye in an N,N' -bis(1-naphthyl)- N,N' -diphenyl-1,1'-biphenyl-4,4'-diamine (NPB) matrix. The dispersion relation can be obtained from the maxima in transmission. The black lines show fits to the dispersion to Equation 5. The solid and dashed yellow lines show the uncoupled photon and exciton dispersion, respectively. The color scale corresponds to the upper polariton branch. Panel b adapted with permission from Reference 44; copyright 2014 John Wiley and Sons.

the excitation of polaritons can be observed as minima and maxima in reflection and transmission, respectively. Physically, these minima and maxima can be considered to be due to the excitation of polaritons and interference with the reradiated field. The full dispersion relation can be obtained by measuring the energy of these minima or maxima as a function of angle using a goniometer.

A more convenient approach to measure the polariton dispersion is Fourier-space imaging. Here, a lens is placed one focal length, f , from the entrance slit of an imaging spectrometer, as illustrated in **Figure 2a**. The lens projects the emission into the far field, so that each position along the entrance slit axis corresponds to a value of the in-plane wavevector (or angle). The spectrograph then disperses the incoming light perpendicular to the slit, so one obtains the entire dispersion relation in a single measurement. An example showing transmission from a squaraine:NPB microcavity [where NPB is N,N' -bis(1-naphthyl)- N,N' -diphenyl-1,1'-biphenyl-4,4'-diamine] is given in **Figure 2b** (see 44). The lower polariton (LP) and upper polariton (UP) branches correspond to maxima in the transmission contour plot (note that a logarithmic color scale is used for the UP). Asymmetry in the visibility of the LP and UP often occurs due to asymmetric (and inhomogeneously broadened) lineshapes as well as background absorption from higher-energy resonances.

To probe condensation, angle-resolved photoluminescence is most useful. The photoluminescence intensity for each k can be related to the polariton population using $I_{PL} \propto n_{\pm}(k)|U_{\pm}(k)|^2/\tau_{\pm}(k)$, where $n_{\pm}(k)$ and $\tau_{\pm}(k)$ are the populations and lifetimes of the LP and UP at in-plane wavevector k .

3. POLARITON CONDENSATION AND LASING

3.1. Bose–Einstein Condensation

Textbook BEC occurs when the density of a gas of bosons is high enough that the chemical potential reaches the bottom of the dispersion. Considering particles in d dimensions with a dispersion

$\epsilon_k = \hbar^2 k^2 / 2m$, we can write the particle number density for the Bose–Einstein distribution as

$$n = \int \frac{d^d k}{(2\pi)^d} \frac{1}{\exp[(\epsilon_k - \mu)k_B T] - 1}. \quad 6.$$

In three dimensions, for $\mu \rightarrow 0$, there is a finite asymptote to n ; that is, $n^{3D}(\mu = 0) = (mk_B T / 2\pi \hbar^2)^{3/2} \zeta(3/2)$, where $\zeta(3/2) \approx 2.61$ is the Riemann zeta function. For densities above this value, the continuum approximation for the density of states fails, and a macroscopic fraction of particles occupy the ground state.

The above holds for a noninteracting Bose gas in three dimensions. In two dimensions, Equation 6 diverges as $\mu \rightarrow 0$, so any density or temperature is compatible with a noncondensed gas, and no transition is expected. However, for an interacting Bose gas, this is not so; the interacting two-dimensional Bose gas undergoes a phase transition at low temperatures to a state that shows order, but not BEC (5). The transition to this low-temperature ordered state is governed by the binding of vortex-antivortex pairs and is known as the Berezinskii–Kosterlitz–Thouless transition (5).

3.2. Lasing

The above summarizes the thermal limit of coherence. The opposite limit is lasing. In a textbook laser, coherence arises by stimulated emission of radiation into a macroscopically occupied photon mode. To describe this, one can find a semiclassical equation of motion for the number of photons, n , in the lasing mode (45):

$$\partial_t n = \frac{Nx\gamma_\downarrow 2g^2(n+1)}{\gamma_\downarrow \gamma_t + 4g^2(n+1)} - \kappa n. \quad 7.$$

In Equation 7, the gain medium is modeled as N two-level systems, with coupling g to the cavity mode, decay rate γ_\downarrow , and total linewidth (including dephasing) γ_t . External pumping of the gain medium is parameterized by $x = (\gamma_\uparrow - \gamma_\downarrow) / (\gamma_\uparrow + \gamma_\downarrow)$. With no pumping, $x = -1$, and with strong pumping, $x = +1$. Photons leak out at rate κ . A necessary condition for lasing is $x > 0$, so the first term provides gain rather than loss of photons. This corresponds to population inversion where stimulated emission becomes more likely than absorption of light.

The semiclassical theory describes both stimulated and spontaneous emission, as seen by the appearance of $n + 1$ in the emission rate. The significance of spontaneous processes is characterized by $\beta = 4g^2 / \gamma_\downarrow \gamma_t$ —the fraction of excited molecules that emit into the cavity mode. To have a sharp lasing transition requires $\beta \ll 1$, so that below threshold, most excitations are lost without emitting into the lasing mode, while above threshold, stimulated scattering changes this. If β is not small, the lasing mode is always efficiently populated, and no threshold exists. One can see this by solving Equation 7, finding

$$n = \frac{1}{2\beta} \left[\frac{x}{x_c} - 1 + \sqrt{\left(\frac{x}{x_c} - 1\right)^2 + 4\beta \frac{x}{x_c}} \right], \quad 8.$$

where $x_c = \kappa \gamma_t / 2g^2 N$ is the threshold pumping. When $\beta = 0$, there is a sharp transition from $n = 0$ for $x < x_c$ to $n \propto (x/x_c) - 1$. At nonzero β , this transition is smeared out.

3.3. Beyond Single Mode: The Complex Gross–Pitaevskii Equation

When comparing equilibrium BEC, polariton condensation, and regular lasing, there are many ways to interpolate between them. One can distinguish weak-coupling versus strong-coupling

lasing, or equilibrium versus nonequilibrium steady states. A third distinction is single-mode versus multimode operation. Equilibrium BEC, involving occupation of various \mathbf{k} states, is intrinsically multimode. In contrast, the laser model above is single mode. A single-mode picture is appropriate if the laser resonator has well-separated optical modes and only a single mode is resonant with the gain medium. For planar microcavities, this is not the case—there is a continuum of photon modes corresponding to different in-plane wavevectors. In real space, this means one must consider the spatial function $\psi(r)$.

The equations governing $\psi(r)$ for a laser (46) and a polariton condensate (4) can in various limits reduce to the complex Gross–Pitaevskii equation (cGPE) (5, 47),

$$i\partial_t\psi = -\frac{\hbar^2}{2m}\nabla^2\psi + V(r)\psi + U|\psi|^2\psi + i(P_{\text{eff}} - \kappa - \Gamma|\psi|^2)\psi. \quad 9.$$

The terms on the right-hand side of this equation fall into two classes. The first three terms—the kinetic, potential, and interaction terms—correspond to the standard GPE (5). The interaction describes the polariton blueshift, increasing energy with polariton density. Such interactions arise from the exchange part of the Coulomb (i.e., dipole-dipole) interaction between excitons (48) and from the exciton saturation (i.e., reduction of coupling strength with increasing density). For Frenkel excitons in organic materials, the small exciton reduces the first of these effects. Polariton interactions in organic materials have been explored recently (27).

The last three terms in Equation 9 describe dissipative processes, that is, pumping, loss, and nonlinear loss. A more sophisticated model (49) of pump and decay can be written as

$$i\partial_t\psi = -\frac{\hbar^2}{2m}\nabla^2\psi + V(r)\psi + (U|\psi|^2 + 2U_{\text{R}n})\psi + i(R(n) - \kappa)\psi, \quad 10.$$

$$\partial_t n = P(r) - \gamma_{\text{R}}n - R(n)|\psi|^2. \quad 11.$$

Here $n(r)$ is the density of an excitonic reservoir, and $R(n)$ is a density-dependent rate of scattering into the condensate; one can approximate $R(n) \simeq R_0 n$. The rate $P(r)$ describes pumping, and γ_{R} is the nonradiative decay rate of the reservoir. The term U_{R} captures the polariton blueshift due to reservoir density (where the reservoir consists of exciton-like states). This model reduces to the cGPE in the limit $\gamma_{\text{R}} \gg \kappa, R_0$, where the reservoir can be adiabatically eliminated—this condition often fails for polariton condensates (50, 51). The similarity of the cGPEs for BECs, lasers, and polariton condensates suggests that similar phenomenology will arise in these cases. There are nonetheless some large-scale features that can be quite sensitive to details of the rates appearing in the effective model (50).

3.4. Observing Polariton Condensation

The typical polariton condensation experiment involves nonresonant pumping (at energies above the exciton), creating an initial population of a reservoir of dark exciton states, such as those described below Equation 3, that subsequently relax into polariton states. Polariton condensation is distinguished by several features.

First and foremost, above a threshold density, a sharp increase in spatial and temporal coherence is observed. This is seen as reduced linewidth and redistribution of the photoluminescence toward the bottom of the LP branch.

Second, there is a sharp nonlinear increase of the emission from $k = 0$ above threshold. Below threshold, dark excitons have many decay pathways: scattering into LP states, near-field energy transfer to other molecules, radiation into weakly coupled modes (e.g., leaky modes of the

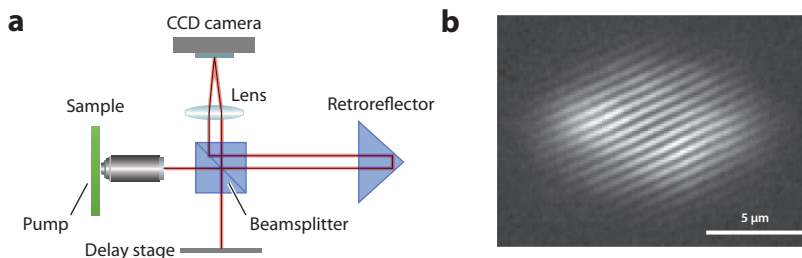


Figure 3

(a) Michelson interferometer, where one arm has been replaced with a retroreflector. One mirror is placed on a delay stage to allow variation of the phase delay or to measure temporal coherence. A lens focuses both images onto a charge-coupled device (CCD) camera. The visibility of the fringes at each point in the interferogram is related to the correlation function between the observation point and its centrosymmetric conjugate. (b) Interferogram of an organic polariton condensate measured with a Michelson interferometer in the retroreflector configuration. Panel *b* adapted with permission from Reference 23; copyright 2015 American Physical Society.

dielectric mirrors or in-plane waveguided modes), and nonradiative decay. However, final-state stimulation, with a rate $\propto(n + 1)$ (see **Supplemental Appendix**) accelerates scattering to $k = 0$ to a point where it exceeds the rates of other decay pathways.

Third, most experiments show a blueshift due to U and U_R . Because the main nonlinearity in most organic microcavities comes from a reduction of the ground-state occupation due to pumping, the blueshift depends on the total population near threshold. If this blueshift is too large, it can indicate a transition to weak coupling.

In inorganic condensates, various signatures are used to distinguish strong- versus weak-coupling lasing. These include whether the effective mass of the dispersion is that of a photon or a polariton (52) and the presence or absence of Zeeman splitting in a magnetic field (53–55). In many inorganic materials, one sees two sequential thresholds, corresponding to polariton lasing and photon lasing (56–60), as strong coupling is suppressed at strong driving. Photon and polariton lasing differ in their mechanism, and hence in their threshold powers. Textbook lasing involves emission into and absorption from the photon mode. In strong coupling, the normal modes are polaritons, so rather than emission, one should discuss scattering from the dark excitonic reservoir to bright polaritonic states (61–64). A mechanism that populates polariton modes in organic cavities, termed radiative pumping, is similar to emission, but with the final state being a polariton. In this case, an electronic transition that is not strongly coupled—e.g., a vibronic sideband, localized state, or defect—radiatively pumps the polariton (65).

As mentioned above, the reduced linewidth and k -space distribution above threshold indicate increased temporal and spatial coherence. Probing coherence more accurately requires interferometry to measure the first-order field correlation function, $\langle \hat{\psi}^\dagger(\mathbf{r}, t) \hat{\psi}(\mathbf{r}', t') \rangle$. Because the emitted photons preserve the phase of the polariton field, interferometric measurements can be performed on the emitted light. A standard Michelson interferometer can measure the temporal correlation function (i.e., $\mathbf{r} = \mathbf{r}'$). Measuring spatial correlation functions requires more care. Most experiments use a variant of the Michelson or Mach–Zehnder interferometer. The Michelson interferometer is modified by replacing the mirror in one arm with a retroreflector, as shown in **Figure 3a** (66). The retroreflector inverts the image so that each point \mathbf{r} of the interferogram is related to the correlation function between the field at \mathbf{r} and $\mathbf{r}' = -\mathbf{r}$. The correlation function is obtained via the fringe visibility. **Figure 3b** shows a typical interferogram above the condensation threshold for the material ter(9,9-diarlylfuorene) (TDAF) (described in Section 4). Some spatial

Supplemental Material >

coherence $>10\ \mu\text{m}$ is immediately seen from the fringe visibility. A more versatile approach is the use of a Mach–Zender interferometer, where in one arm, a telescope and pinhole select and magnify a specific region \mathbf{r} of the condensate (67). This point then serves as a phase reference, and the field is combined with an image of the entire condensate to create an interferogram.

4. MATERIALS

Polariton condensation has been seen in a range of organic materials. These include organic crystals, disordered molecular thin films, polymers, and fluorescent proteins. **Figure 4** shows examples of materials used to realize organic polariton condensates. In this section, we review many of these experimental realizations and the corresponding material sets. **Table 1** summarizes the properties of reported organic polariton lasers to date.

4.1. Organic Crystals

Most early work on organic microcavities focused on either low-molecular-weight emitters or J-aggregated cyanine dyes in host matrices (14, 15, 17, 71, 72). However, the first demonstration of polariton condensation used an organic single crystal. For some time, it was thought that the large static disorder in existing structures would hinder organic polariton BEC. First, the disorder

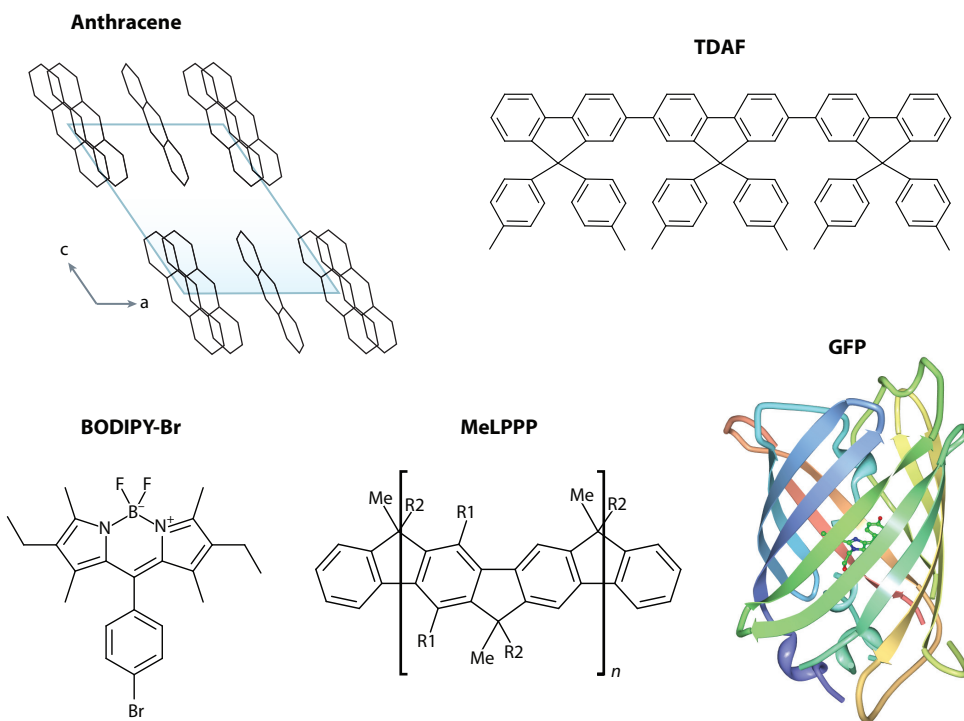


Figure 4

Some of the organic materials showing polariton condensation. A perspective view of the anthracene crystal structure is shown from the ac plane. In MeLPPP, R1 is n -hexyl and R2 is 1,4-decylphenyl. The chromophore in GFP is shown along with the β -barrel. Abbreviations: BODIPY-Br, brominated boron dipyrromethene; GFP, green fluorescent protein; MeLPPP, methyl-substituted ladder-type poly(paraphenylene); TDAF, ter(9,9-diaryl)fluorene.

Table 1 Parameters from reported organic polariton laser experiments

Material	λ (nm)	Ω_R (meV)	DBR pairs (top/bottom)	τ_p (ps)	P_{th} or I_{th}	Reference(s)
Anthracene	420	256	12/12	0.1–0.2	$320^a \mu\text{J}/\text{cm}^2$	21, 68
TDAF	415	600	9/9	0.15	$13\text{--}27^a \mu\text{J}/\text{cm}^2$	22, 23, 69
MeLPPP	475	116	6.5/9.5	0.16	$130\text{--}500 \mu\text{J}/\text{cm}^2$	28, 29
BODIPY-Br	565	91	8/10	0.13	$527 \mu\text{J}/\text{cm}^2$	24, 25
BODIPY-G1	550	114	8/10	0.1	$6 \text{ mJ}/\text{cm}^2$	27, 70
Pentafluorene	437	500	6.5/10.5	0.06	$12^a \mu\text{J}/\text{cm}^2$	26
PFO	520	437	6.5/10.5	0.19	$27 \mu\text{J}/\text{cm}^2$	30
eGFP	520	194	14/14	0.1	$300^b \text{ kW}/\text{cm}^2$	31
mCherry	640	266	10.5/10.5	2	$600^b \text{ kW}/\text{cm}^2$	32

Abbreviations: BODIPY-Br, brominated boron dipyrromethene; BODIPY-G1, nonbrominated boron dipyrromethene; DBR, distributed Bragg reflector; eGFP, enhanced green fluorescent protein; MeLPPP, methyl-substituted ladder-type poly(paraphenylene); PFO, poly(9,9'-dioctylfluorene); TDAF, ter(9,9-diarylfuorene).

^aThese correspond to the absorbed fluence at threshold. In all reports, pumping is in the transparency window of the DBRs, so the absorbed and incident fluence differ by at most a factor of ~ 2 .

^bNote the deliberate use of threshold irradiance instead of fluence for experiments with long excitation pulses. In these cases, the exciton density is related not to the fluence but to the product of the peak irradiance with the dark reservoir lifetime.

will localize the polariton wavefunctions for states near $k = 0$ (see 73). Second, disordered films inevitably have many molecules with the wrong dipole moment orientation to couple to a given electric field polarization, lowering the Rabi energy. Third, these misaligned molecules can be a sink for the excited population via Förster transfer. This stimulated work on more ordered and, ultimately, crystalline thin films. In 2004 and 2008, respectively, strong exciton-photon coupling was demonstrated in nanocrystalline films of 3,4,7,8-naphthalenetetracarboxylic dianhydride (NTCDA) and polycrystalline tetracene (17, 74). The latter showed crystalline domains of several micrometers, sufficient to observe signatures of the exciton band structure and anisotropy (75). However, the large surface roughness of polycrystalline films makes it challenging to integrate them into high-quality-factor microcavities.

In 2008, two reports demonstrated microcavities containing single crystals of anthracene (21, 76). Recent work has also shown strong coupling with rubrene single crystals (77). The lowest-energy electronic transition in anthracene has its dipole moment along the molecule's short axis, and the presence of two molecules per unit cell leads to a Davydov splitting of the low-lying exciton transition into bands polarized along the **b** direction and in the **ac** plane (78) (see **Figure 4**). In general, the surface of the crystal is oriented parallel to the (001) plane because of its low surface energy. For wavevectors incident on this plane, the Davydov splitting between the **ac** and **b** exciton bands is approximately 200 cm^{-1} . The lowest-lying and strongest transition corresponds to the **b** exciton (79).

Because resonance of the exciton and photon requires precise tuning of the microcavity thickness, Reference 21 introduced a technique to grow large single crystals with nanometric precision over the thickness. The resulting microcavities revealed a strongly anisotropic dispersion due to the two exciton resonances and birefringence in the background refractive index (75, 80). For an electric field polarized along the **a** or **b** direction, the coupling strength g with the corresponding exciton is maximized, and the dispersion shows four polariton branches due to strong coupling to the 0-0, 0-1, and 0-2 vibronic transitions, as shown in **Figure 5a** for the **b** direction. The vibronic transitions in anthracene are apparent in the absorption spectrum shown on the right side of **Figure 5a**.

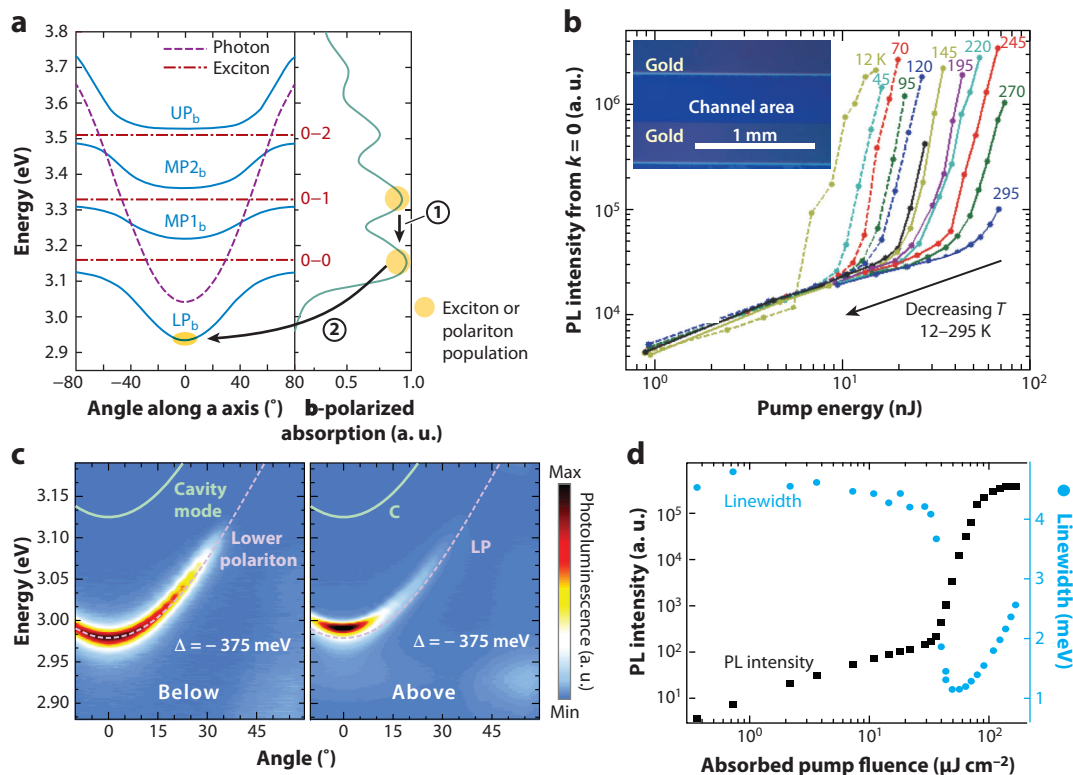


Figure 5

(*a, left*) Dispersion of the anthracene microcavity for polarization along the **b** axis showing lower, middle, and upper branches. The bare photon and exciton energies are shown as dashed lines. (*a, right*) Absorption spectrum and diagram of the lasing mechanism: (①) Internal conversion populates the dark exciton reservoir; (②) emission of vibration causes relaxation to $k = 0$. Numbers in red label transitions by initial and final vibrational excitation number. (*b*) Power dependence of emission at $k = 0$ at various temperatures. The inset shows an image of the microcavities. (*c*) Contour plot of the angle-resolved PL from a TDAF microcavity below (*left*) and above (*right*) threshold showing the collapse to $k = 0$. The bare cavity mode is identified in black. (*d*) Power dependence of PL and linewidth at $k = 0$. Abbreviations: LP, lower polariton; MP, middle polariton; PL, photoluminescence; TDAF, ter(9,9-diarylfuorene); UP, upper polariton. Panel *a* adapted with permission from Reference 20; copyright 2013 Springer Nature. Panel *b* adapted with permission from Reference 68; copyright 2015 American Physical Society. Panels *c* and *d* adapted with permission from Reference 22; copyright 2013 Springer Nature.

The anthracene microcavity structures had a (calculated) empty cavity quality factor, $Q = \omega/\Delta\omega$, where $\Delta\omega$ is the cavity mode linewidth, of $\sim 6,000$. An optical micrograph of the completed structure is shown in the inset of **Figure 5b**. From the photoluminescence linewidth of $\Delta E_{LP} \sim 3.5\text{--}5.5$ meV, the polariton lifetime can be estimated to be $\tau_p = \hbar/\Delta E_{LP} \sim 150\text{--}200$ fs. This is considerably shorter than the greater-than-picoseconds lifetimes typical of inorganic microcavities, but it turns out to be sufficient to achieve condensation for many organic materials. In anthracene, condensation was observed only when the cavity thickness was adjusted such that the LP minimum, at $E_{LP}(0) = 2.94$ eV, is precisely tuned one vibrational energy $E_{\text{vib}} = 173$ meV below the zero-phonon-line energy (i.e., the undressed fluorescence peak), E_{0-0} . This is shown schematically in **Figure 5a**.

When the pump power is increased for this detuning, one finds a threshold, P_{th} , beyond which the signatures of condensation listed in Section 3.4 are seen. The superlinear increase in intensity is

shown in **Figure 5b**. Evidence of stimulated scattering is also observed via the photoluminescence lifetime, which reduces drastically beyond the threshold. Two possible mechanisms can explain the reduction of the condensation threshold at the resonance between the LP and the vibrational sidebands of the exciton—that is, when $E_{\text{LP}}(0) = E_{0-0} - E_{\text{vib}}$. Relaxation from the dark exciton reservoir to the $k = 0$ LP can be enhanced either by the emission of a vibrational phonon or via radiative pumping of the LP by the 0-1 fluorescence peak. A model treating strong coupling as coming from only the zero-phonon line (81) allows one to calculate the rates of these two processes.

A few additional interesting features emerged from the anthracene experiments. From modeling, a bimolecular annihilation coefficient ~ 50 times smaller than the reported value was found (81). Suppressed radiation from the dark exciton reservoir combined with a modification of the optical density of states may explain this effect. Because of the high intrinsic photoluminescence quantum yield (PLQY) of most organic laser materials, their laser threshold is typically nearly independent of temperature. In contrast, for anthracene, a decrease in the threshold by nearly a factor of 10 is found when cooling from room temperature to 12 K, as shown in **Figure 5b** (from 68). The origin of this effect has not been investigated in detail but may in part be related to an increase in polariton lifetime due to the dramatic exciton linewidth narrowing that occurs in anthracene upon cooling. Finally, in unpublished experiments, nonlinear behavior could also be seen higher up in the dispersion relation (i.e., away from $k = 0$), at the energy corresponding to $E_{0-0} - E_{\text{vib}}$. Although the powers required for these observations were higher than those required for $k = 0$ condensation, this clearly highlights the importance of the vibronic replica in the relaxation process and the fact that relaxation within the LP dispersion is inefficient due to the short polariton lifetime.

4.2. Small Molecules

Low-molecular-weight organic molecules are considerably easier to process into disordered or polycrystalline thin films than into single crystals. The most commonly used fabrication techniques are spin coating and vacuum sublimation (82). Both allow for the fabrication of neat (undoped) films or doped films where the dye is embedded within a host matrix. The films often show some orientational alignment [e.g., molecules lying mostly flat on the substrate (83)] and even form small crystalline domains, but the in-plane alignment of domains is random in the absence of any directed templating.

One of the most studied polariton lasing materials is the fluorene oligomer TDAF, an bipolar blue organic light-emitting diode material that can be processed from both solution and vacuum (84). It shows some degree of in-plane anisotropy, due to the long molecules lying mostly parallel to the substrate (85). This orientation leads to a larger absorption coefficient for in-plane polarization, compared with out-of-plane, and consequently to a larger Rabi energy (which is angle dependent for transverse-magnetic polarization). **Figure 5c** shows the redistribution of the PL intensity toward the bottom of the LP branch when a condensate is formed. The threshold for condensation in TDAF is 10 times lower than in anthracene, as shown in **Figure 5d** (see **Table 1**). Reduced bimolecular annihilation, the slightly longer polariton lifetime, and the larger Rabi energy may all contribute to lowering the threshold. One peculiarity of TDAF, in contrast to the crystalline case (where emission is always polarized), is the polarization behavior. Because of in-plane disorder, the $k = 0$ emission is unpolarized below threshold. Above threshold, however, the condensate polarization spontaneously aligns to the pump. This indicates that stimulated scattering becomes faster than depolarization mechanisms such as internal conversion and energy transfer. Follow-up work found a threshold as low as $P_{\text{th}} = 13 \mu\text{J}/\text{cm}^2$ when the LP is resonantly pumped (69).

The narrow linewidth of the condensate emission also paints a much clearer picture of the nonlinearity than in anthracene. In **Figure 5c**, one can clearly resolve the blueshift of the dispersion above threshold. This blueshift results from ground-state depletion, reducing the Rabi energy $\Omega_R = g\sqrt{N}$ due to its N dependence. Under nonresonant pumping, the missing ground-state population is mostly in the dark exciton reservoir. This induces an effective repulsive interaction U_R between dark excitons and polaritons (22). Beyond P_{th} , the dark exciton population is clamped, and the LP population increases significantly. One can thus assign the slope of the blueshift above threshold to a polariton-polariton interaction, which also originates from ground-state depletion. Different measurements of this interaction strength have found $U = 10^{-3} \mu\text{eV} \mu\text{m}^2$ (23, 86).

In TDAF, there is a clear transition from a blurred interferogram with uncorrelated phases below P_{th} to an interferogram showing well-resolved fringes over nearly the entire condensate area above P_{th} (see **Figure 3b**) (23). The measured coherence time was $\tau_c = 0.8$ ps at $P = 1.5P_{th}$, as shown in **Figure 6a**, which coincides well with the estimated lifetime of the condensate under impulsive pumping. This is dictated by how quickly the dark exciton reservoir is depopulated to a value below threshold. The degree of spatial coherence increases with power above threshold and can be quantitatively measured as shown in **Figure 6b,c**. One must take care, however, when interpreting the spatial decay of these correlation functions, as they are influenced by the pump intensity distribution. Measurements with very large spots or a flat-top pump show much weaker phase contrast and spatial structure in the intensity profile due to the presence of dynamic instabilities (50). The combination of a repulsive polariton-exciton interaction and gain leads to spatial hole burning in the dark exciton reservoir density and thus to a fragmentation of the condensate.

An important target for materials exploration is lowering the polariton lasing threshold. Recent efforts have focused on materials with a high PLQY so that fewer decay channels compete with lasing. A closely related oligofluorene is pentafluorene, with a film PLQY around 90%. Experiments (26) with this material have shown a lasing threshold at $P_{th} = 17 \mu\text{J}/\text{cm}^2$, corresponding to an absorbed fluence of only $P_{th} = 11.7 \mu\text{J}/\text{cm}^2$.

Recent work has also shown condensation in thin films of high-PLQY brominated boron dipyrromethene (BODIPY-Br) dye dispersed in a polystyrene matrix (25). Diluting the film reduces aggregation-induced concentration quenching and bimolecular annihilation but also leads to a smaller Ω_R . **Figure 7** shows the power dependence near $k = 0$ and the k -space PL below

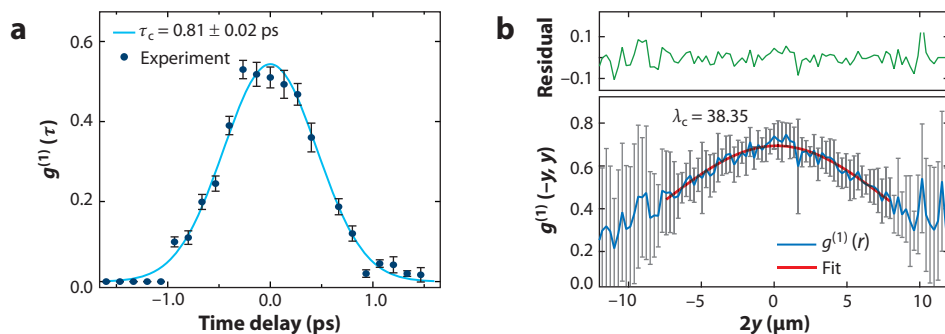


Figure 6

(a) First-order temporal coherence of a ter(9,9-diarylfuorene) (TDAF) microcavity from a Michelson interferometer. The coherence time corresponds roughly to the condensate emission pulse duration plotted for $1.7P_{th}$. (b) A vertical slice of the first-order spatial correlation function across the condensate center for $1.9P_{th}$. The coherence length $\lambda_c = 38 \mu\text{m}$ is obtained from a Gaussian fit (red line). Figure adapted with permission from Reference 23; copyright 2015 American Physical Society.

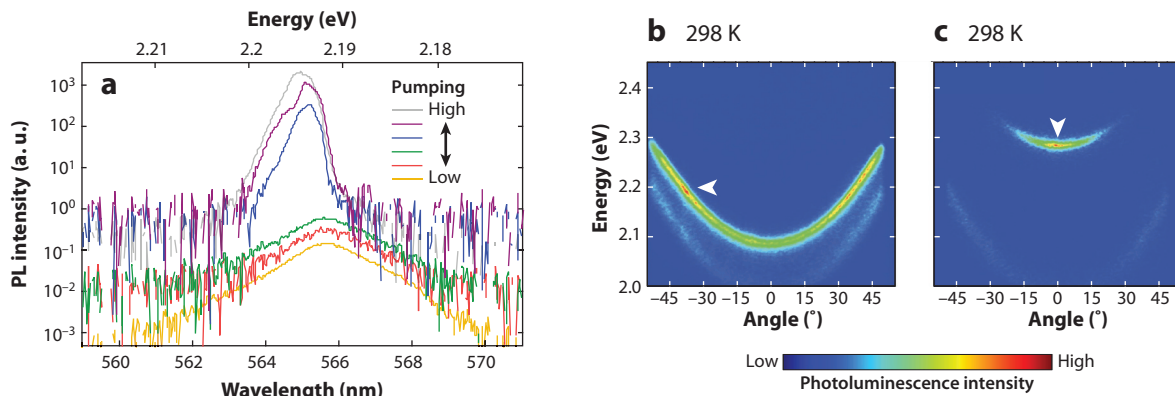


Figure 7

(a) Power dependence of the emission spectrum from $k = 0$ showing the onset of condensation. (b,c) Angle-resolved photoluminescence (PL) below threshold for a brominated boron dipyrromethene (BODIPY-Br) cavity with detunings of (b) -290 meV and (c) -106 meV. Note how the emission is peaked near 2.2 eV in panel b but at the lower polariton branch minimum in panel c (marked with white arrowheads). Panel a adapted with permission from Reference 25; copyright 2017 John Wiley and Sons. Panels b and c adapted with permission from Reference 24; copyright 2016 John Wiley and Sons.

threshold for different detunings. Studies of BODIPY-Br microcavities have shown that the dominant mechanism for populating the LP in this material consists of radiative pumping from weakly coupled excimers (24). The qualitative difference in occupation along the LP branch between **Figures 7b** and **7c** can be reproduced by a model where the LP is being radiatively pumped from a single state near 2.09 eV, which coincides well with the excimer emission observed in bare films. In this scenario, dark excitons energy-transfer to molecular dimers that support excimer formation in the excited state, and excimer emission then populates the LP. One notable difference compared with TDAF is that the BODIPY-Br blueshift increases linearly with excitation fluence instead of showing a difference in slope below and above threshold. Finally, an attractive feature of BODIPY-Br is that it emits yellow coherent light at $\lambda = 565$ nm, a wavelength that is hard to access for inorganic semiconductor lasers.

A similar nonbrominated boron dipyrromethene (BODIPY-G1) dye has been used to study the origin of the blueshift and polarized emission in polariton condensates (27). In Reference 27, the authors conclude that the blueshift is due to a ground-state bleach, and by including the presence of a reservoir of dark molecules (misaligned with the pump beam electric field), they can explain the spontaneous polarization observed when crossing the threshold.

4.3. Polymers

To some extent, conjugated polymer photophysics combines features of small molecules and organic crystals. Exciton bands can form along the polymer chain due to dipole-dipole coupling and superexchange between moieties, while incoherent Förster transfer can lead to interchain energy transfer (36). In spin-coated films, polymer chains typically lie in plane but adopt chain configurations with bends, twists, etc., that lead to an inhomogeneous distribution of chromophores within each chain. Structural defects or chemical impurities within a chain can act as efficient quenching centers for excitons. Ladder-type polymers adopt a nearly rigid one-dimensional geometry that reduces inhomogeneous broadening and allows for long exciton dephasing times at low temperature (87). The methyl-substituted ladder-type polymer poly(paraphenylene) (MeLPPP) is the first

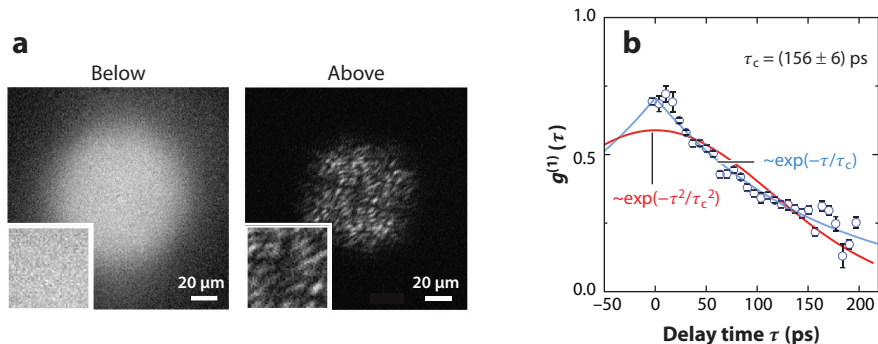


Figure 8

(a) Interferogram measured below (*left*) and above (*right*) threshold for the methyl-substituted ladder-type poly(paraphenylene) (MeLPPP) microcavity using a Michelson interferometer. Note the appearance of a speckle-like interference pattern instead of parallel fringes. Insets represent an enlarged segment ($2\times$ enlargement) of the main image. (b) First-order temporal coherence function measured for a confined mCherry microcavity under long-pulse excitation. Lorentzian and Gaussian fits are shown. Panel *a* adapted with permission from Reference 28; copyright 2013 Springer Nature. Panel *b* adapted with permission from Betzold et al., *ACS Photonics* 2020 7:384–92, <https://doi.org/10.1021/acsp Photonics.9b01300> (32); copyright 2019 American Chemical Society.

spin-coated material where polariton condensation was observed (28). The electrical and optical properties of MeLPPP have been extensively studied (88–90).

Plumhof et al. (28) demonstrated condensation by embedding a 35-nm-thick film of MeLPPP in a dielectric microcavity; they observed strong coupling to both the 0-0 and the 0-1 transition. As the pump intensity increases, a peak emerges from the blue edge of the $k = 0$ photoluminescence, which slowly blueshifts with increasing pump fluence. This peak is assigned to the condensate. MeLPPP also shows conventional optical gain, but interestingly, the wavelength of the condensate emission (474 nm) is just beyond the range where conventional optical gain has been observed (480–573 nm) (90). These microcavities also show an interesting temperature dependence, with the emission maximum being near $k = 0$ at room temperature but at higher k when the temperature is lowered. Inefficient pumping of the states near $k = 0$ at low temperature is also reflected in the threshold behavior. When the temperature is lowered to below 50 K, the threshold increases by more than an order of magnitude. The relaxation dynamics in MeLPPP microcavities are not yet understood. Indeed, even thin films of this material show a strong temperature dependence of the vibronic photoluminescence intensities combined with a large redshift of the peak positions. The interferograms from this work are also distinct from those in other reports—clear structure emerges beyond threshold, but the speckle-like pattern does not show a smoothly varying phase pattern (see **Figure 8a**). This might be due to the more disordered nature of the spin-coated polymer films, compared with other materials, or to the presence of dynamic instabilities resulting from the choice of excitation conditions.

Follow-up work has shown condensation in confined lateral structures in an open microcavity by etching micrometer-sized concave defects on one of the mirror substrates. The two sides of the microcavity—the planar DBR and film, and the mirror with defect—are brought together with nanopositioners to form the complete microcavity (29). Confinement from the Gaussian defect leads to the formation of zero-dimensional confined Laguerre–Gaussian modes, and condensation occurs in the lowest-lying Laguerre–Gaussian mode. In this case, clear interference fringes are visible in the confined geometry, highlighting the high degree of spatial coherence within the micrometer-sized confinement region.

A recent report showed polariton lasing in the polymer poly(9,9'-dioctylfluorene) (PFO) (see **Table 1**). In contrast to MeLPPP, this material is less rigid and thus shows higher disorder typical of conjugated polymers (30).

4.4. Fluorescent Proteins

Polariton lasing has also been observed in biologically derived fluorescent proteins. A prototypical example of such a protein is green fluorescent protein (GFP), which was first isolated from the jellyfish *Aequorea victoria* (91). Because of its low toxicity, high luminescent yield, and good photostability, it has found considerable use in fluorescence microscopy. Most fluorescent proteins consist of a chromophore surrounded by a cylindrical β -barrel, as shown in **Figure 4**. The barrel is composed of several β -sheets, formed by long polypeptide chains. These isolate the chromophore from its environment while also hindering rotational motion. This can reduce internal conversion and/or intersystem crossing and increase fluorescent yield. The first polariton condensate made by using a fluorescent protein was fabricated from enhanced GFP films of 500-nm thickness spin-coated onto a highly reflecting DBR (31). The structure was then completed by mechanically laminating a second DBR on top of the film. This leads to a multimode structure and natural variations in the cavity thickness, ranging from 1,500 to 4,500 nm. One remarkable advance from this work is the use of longer nanosecond pulses (7 ns) for optical pumping. This is possible as a result of the low threshold and the greatly reduced exciton-exciton annihilation between the β -sheet-protected chromophores. At large pump densities, a second threshold (P_2) is observed in this sample, which is ascribed to conventional photon lasing in a lower-energy cavity mode. To date, this is the only organic material where such a second threshold has been observed.

Recently, polariton condensation was observed from the fluorescent protein mCherry in a three-dimensional confined geometry (32), obtained by fabricating small hemispherical indentations on the glass substrate supporting one of the mirrors. The high quality of the structure leads to a remarkable polariton lifetime of 2 ps, and the long pulses allow for an interferometric measurement of the polariton temporal coherence, not limited by the duration of the condensate emission. The authors find $\tau_c = 156$ ps at $P = 1.7P_{th}$, as shown in **Figure 8b**.

5. THEORETICAL MODELS

Here we discuss various models used for polariton lasing. A more complete discussion of how these models can then be treated is presented in the **Supplemental Appendix**.

Supplemental Material >

5.1. Weakly Interacting Dilute Bose Gas

A widely used model for BECs of atoms and inorganic polaritons concerns bosonic particles, described by annihilation operators \hat{b}_k , and is given by

$$H = \sum_{\mathbf{k}} \epsilon_{\mathbf{k}} \hat{b}_{\mathbf{k}}^{\dagger} \hat{b}_{\mathbf{k}} + \frac{U}{V} \sum_{\mathbf{k}, \mathbf{k}', \mathbf{q}} \hat{b}_{\mathbf{k}+\mathbf{q}}^{\dagger} \hat{b}_{\mathbf{k}'-\mathbf{q}}^{\dagger} \hat{b}_{\mathbf{k}} \hat{b}_{\mathbf{k}}. \quad 12.$$

The dispersion ϵ_k is taken either to be quadratic ($\epsilon_k = k^2/2m_{pol}$) or to follow the LP dispersion (Equation 5). The interaction U describes the nonlinear polariton blueshift and is here approximated as a contact interaction independent of \mathbf{q} .

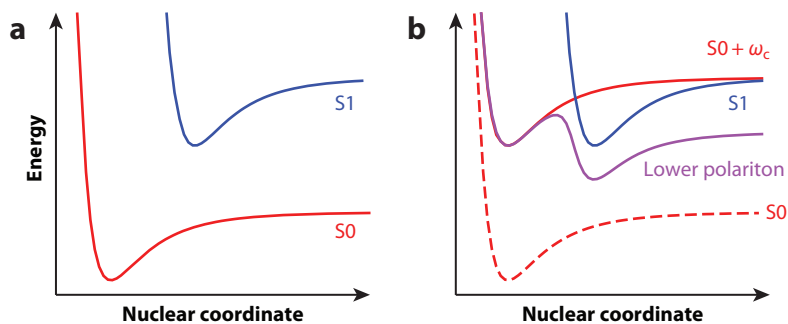


Figure 9

Diagram of potential energy surfaces. (a) S0 and S1 levels; these label the first two singlet states of the molecule. (b) Polaritonic surface, hybridizing the S0 level with the energy-shifted S1 level.

5.2. Two-Level Systems

For Frenkel excitons, a two-level system approach, such as the generalized Tavis–Cummings model (Equation 4), is a more natural starting point. The Pauli operators σ_n^\pm in this model may be considered as paulions (92), which obey Pauli exclusion, but unlike for fermions, operators on different sites commute. Various approaches exist to relate such models to interacting bosons, such as the Holstein–Primakoff transformation, $\sigma^+ = b^\dagger \sqrt{1 - b^\dagger b}$ (restricting $b^\dagger b \leq 1$), or via an alternate transformation (92), $\sigma^+ = b^\dagger \sqrt{\frac{(-2)^n}{(1+n)!} (b^\dagger)^n (b)^n}$. These transforms give effective weakly interacting dilute Bose gas models, with interactions originating from the saturability of the two-level systems (92). Another approach (93) is based on composite boson theory for Frenkel excitons, including electron-hole exchange processes. One can also work directly with the full model with spins, particularly where mean-field theory holds (94).

5.3. Vibrational Sidebands and the Tavis–Cummings–Holstein Model

The absorption and emission spectra of organic materials are more complex than those of a two-level system. Various photophysical processes are responsible for this, in particular dressing by vibrational modes. These modes come from the potential energy surface of the nuclear coordinates. To understand their effect, one must consider the kinetic and potential energies of both electrons and nuclei, the interaction between them, and their coupling to light. Considering for simplicity a single-cavity-mode, single-molecule model, we have

$$H = T_e(\hat{p}_e) + T_n(\hat{p}_n) + V(\hat{r}_e, \hat{r}_n) + \omega_c a^\dagger a + \mathbf{d}(\hat{p}_e, \hat{p}_n) \cdot \mathbf{A}_0(a + a^\dagger). \quad 13.$$

Here $V(\hat{r}_e, \hat{r}_n)$ includes both internuclear and electron-nuclear interactions. The matter-light coupling involves a dipole element that can include both electronic and nuclear operators. The constant \mathbf{A}_0 describes the field strength (vector potential) of a single photon.

For weak matter-light coupling, one can make the standard Born–Oppenheimer approximation—a separation of timescales between fast electron dynamics and slow nuclear dynamics. This leads to the diagram shown in **Figure 9a**. When considering strong matter-light coupling, a question arises regarding the matter-light coupling in the Born–Oppenheimer approximation (95, 96): Should matter-light coupling be treated as fast or slow? As discussed in Reference 95, in the limit when the matter-light coupling is the largest scale (larger than the vibrational reorganization energy), it clearly is part of the fast degrees of freedom. In that

case, following the Born–Oppenheimer approximation, one can diagonalize the electronic and optical part of the Hamiltonian at a given nuclear coordinate, giving polaritonic potential energy surfaces, as shown in **Figure 9b**. In plotting **Figure 9b**, the Frank–Condon approximation is also made—that is, optical transitions are fast compared with nuclear motion and hence are vertical. We thus see hybridization between (a) the S1 potential energy surface and (b) the S0 energy surface vertically shifted by ω_c .

So far, we have assumed a generic nuclear potential energy; however, this can often be approximated as quadratic. Assuming the dipole element depends only on the electronic state (i.e., the vibrational mode is not infrared active), we may write

$$H = \omega_c \hat{a}^\dagger \hat{a} + \sum_n \epsilon \sigma_n^+ \sigma_n^- + g(\sigma_n^+ \hat{a} + \text{H.c.}) + E_{\text{vib}} \left(\hat{b}_n^\dagger \hat{b}_n + \sqrt{S}(\hat{b}_n^\dagger + \hat{b}_n) \sigma_n^+ \sigma_n^- \right). \quad 14.$$

This model, the Tavis–Cummings–Holstein model¹ (97), describes a harmonic oscillator vibrational mode for each molecule coupled to the electronic state. The dimensionless Huang–Rhys parameter S is the offset between the minima in the S0 and S1 states in units of the harmonic oscillator lengthscale. This model considers only a single vibrational mode; however, in many cases, one must include both fast vibrational modes and slow rotational or torsional modes. Models capturing this have recently been discussed in the context of electron transfer processes (98).

5.4. Methods to Model Polariton Condensation

Even once the Hamiltonian is specified, a wide variety of approaches remain to be used, ranging from equilibrium statistical physics (5) to open quantum system theory (99). We briefly summarize here some widely used methods (for further details, see the **Supplemental Appendix**).

Kinetic models describe transitions between a fixed set of normal modes, such as polariton momentum states. These have been applied to organic polariton lasing, using models that include effects of vibrational sidebands (65, 81). Such models explain the enhanced scattering into a polariton state when the splitting between the polariton energy and excitonic reservoir matches a vibrational resonance. A drawback to such methods is that, in general, they assume the normal modes are well defined and unchanging—the spectrum is fixed, and only the occupation changes. This assumption is good deep in the strong-coupling regime, or in weak coupling, but fails at the crossover from strong to weak coupling. To go beyond this, it is necessary to use more general methods of open quantum systems such as the master equation (see **Supplemental Appendix**). An approach based on the Tavis–Cummings–Holstein model driven out of equilibrium (100) is able to recover the results of Reference 81 in strong coupling and to show how this emerges continuously from the weak-coupling limit.

6. CONCLUSIONS

In this review, we introduced polariton condensation and lasing with molecular materials. There now exist a wide variety of such materials showing condensation; however, important questions remain to be addressed. In choosing materials, some features of a good material are known: high PLQY, and strong coupling to vibrational modes to enable thermalization. Other questions remain unclear: Do single-crystal materials significantly reduce the condensation threshold? How

¹In writing this model, we made the rotating wave approximation, neglecting terms that create a photon and excite a molecule, as in the standard Tavis–Cummings model. If we retain counterrotating terms, our model becomes the Dicke–Holstein model.

to realize stronger nonlinear interactions? What routes exist toward thermal-equilibrium organic condensates?

Practically, the ability to electrically create organic polariton condensates would be very attractive. However, prospects for electrical pumping will be hampered by the same elements that have made the realization of electrically pumped organic lasers challenging: low charge carrier mobilities, excited-state absorption from charges, singlets and triplets, bimolecular annihilation between different species, and low thermal conductivity (101). Indirect electrical pumping using inorganic light-emitting diodes or the use of hybrid organic-inorganic microcavities may be more viable to realize turnkey room-temperature condensates (102–104). Such structures could also exploit the large nonlinearity inherent to the inorganic component (105).

Beyond these specific questions, there are several novel directions to explore. One is modification of photophysics. When light couples strongly to some organic materials, it can modify aspects of the photophysics, such as the role of vibrational modes, the role of different molecular chromophores in absorption and emission, and the processes of vibrational relaxation (44, 73, 95, 106). Modifying molecular properties such as internal conversion and/or intersystem crossing dynamics, carrier mobilities, and excited-state absorption may allow one to overcome some difficulties inherent to conventional organic lasers (107–110). Perhaps more interestingly, the existence of a condensate providing a coherent population of polaritons may modify these properties further.

SUMMARY POINTS

1. Polariton condensation—a macroscopic coherent state of polaritons—can be realized in a microcavity device, when it is pumped so as to overcome cavity losses.
2. A wide variety of organic materials have now been studied in this context. These include both crystalline and amorphous materials, showing that it is possible to realize an ordered polariton state even when the underlying material is disordered.
3. From both theory and experiment, the optimal conditions for lasing correspond to maximizing photoluminescence quantum yield (i.e., minimizing nonradiative loss), increasing exciton-vibron coupling sufficiently to allow thermalization, and minimizing cavity losses.
4. From theory, it appears that while threshold pumping decreases with increasing matter-light coupling, most of this behavior can be understood from weak-coupling approaches. The thresholds attained experimentally so far are all higher than the best weak-coupling organic lasers.

FUTURE ISSUES

1. As yet, the realizations of organic polariton condensation are all significantly out of equilibrium. Work is required to move these toward a thermal equilibrium limit.
2. Further understanding is required of what makes for an optimal condensation threshold, including the role of disorder. That is, what should be the design principles to reduce this threshold as far as possible?

3. Many organic materials show a weak polariton nonlinearity, due to the tight binding of the exciton state. Enhancing this nonlinearity is necessary for many applications, including the realization of parametric oscillation and amplification with organic polaritons, as well as for ultimately attaining the quantum blockade regime.
4. For many potential applications, one needs to consider electrical injection and engineering lateral structures in a polariton condensate. While many tools exist for this in inorganic materials, extending this to organics is a significant undertaking.
5. A broad topic for future work regards understanding how internal photophysical processes, such as electronic structure changes or vibrational relaxation, is affected by strong coupling.

DISCLOSURE STATEMENT

The authors are not aware of any affiliations, memberships, funding, or financial holdings that might be perceived as affecting the objectivity of this review.

ACKNOWLEDGMENTS

J.K. acknowledges funding from the Engineering and Physical Sciences Research Council program Hybrid Polaritonics (EP/M025330/1). This work was performed in part at Aspen Center for Physics, which is supported by National Science Foundation grant PHY-1607611. This work was partially supported by a grant from the Simons Foundation. S.K.-C. acknowledges support from the Natural Sciences and Engineering Research Council Discovery Grant program and the Canada Research Chair program.

LITERATURE CITED

1. Pekar S. 1958. The theory of electromagnetic waves in a crystal in which excitons are produced. *Sov. Phys. JETP* 6:785–96
2. Hopfield J. 1958. Theory of the contribution of excitons to the complex dielectric constant of crystals. *Phys. Rev.* 112:1555–67
3. Kavokin AV, Baumberg JJ, Malpuech G, Laussy FP. 2007. *Microcavities*. Oxford, UK: Oxford Univ. Press
4. Carusotto I, Ciuti C. 2013. Quantum fluids of light. *Rev. Mod. Phys.* 85:299–366
5. Pitaevskii LP, Stringari S. 2003. *Bose–Einstein Condensation*. Oxford, UK: Clarendon
6. Sanvitto D, Kéna-Cohen S. 2016. The road towards polaritonic devices. *Nat. Mater.* 15:1061–73
7. Berloff NG, Silva M, Kalinin K, Askitopoulos A, Töpfer JD, et al. 2017. Realizing the classical XY Hamiltonian in polariton simulators. *Nat. Mater.* 16:1120–26
8. Kim NY, Yamamoto Y. 2017. Exciton-polariton quantum simulators. In *Quantum Simulations with Photons and Polaritons: Merging Quantum Optics with Condensed Matter Physics*, ed. DG Angelakis, pp. 91–121. Cham, Switz.: Springer Int.
9. Liew T, Kavokin A, Shelykh I. 2008. Optical circuits based on polariton neurons in semiconductor microcavities. *Phys. Rev. Lett.* 101:016402
10. Ebbesen TW. 2016. Hybrid light–matter states in a molecular and material science perspective. *Acc. Chem. Res.* 49:2403–12
11. Feist J, Galego J, Garcia-Vidal FJ. 2017. Polaritonic chemistry with organic molecules. *ACS Photonics* 5:205–16
12. Ribeiro RF, Martínez-Martínez LA, Du M, Campos-Gonzalez-Angulo J, Yuen-Zhou J. 2018. Polariton chemistry: controlling molecular dynamics with optical cavities. *Chem. Sci.* 9:6325–39

13. Agranovich VM. 1968. *The Theory of Excitons*. Moscow: Nauka
14. Lidzey DG, Bradley DDC, Skolnick MS, Virgili T, Walker S, Whittaker DM. 1998. Strong exciton-photon coupling in an organic semiconductor microcavity. *Nature* 395:53–55
15. Lidzey DG, Bradley DDC, Virgili T, Armitage A, Skolnick MS, Walker S. 1999. Room temperature polariton emission from strongly coupled organic semiconductor microcavities. *Phys. Rev. Lett.* 82:3316–19
16. Lidzey DG, Bradley DDC, Armitage A, Walker S, Skolnick MS. 2000. Photon-mediated hybridization of Frenkel excitons in organic semiconductor microcavities. *Science* 288:1620–23
17. Holmes RJ, Forrest SR. 2004. Strong exciton-photon coupling and exciton hybridization in a thermally evaporated polycrystalline film of an organic small molecule. *Phys. Rev. Lett.* 93:186404
18. Tischler JR, Bradley MS, Bulović V, Song JH, Nurmikko A. 2005. Strong coupling in a microcavity LED. *Phys. Rev. Lett.* 95:036401
19. Tischler JR, Bradley MS, Zhang Q, Atay T, Nurmikko A, Bulović V. 2007. Solid state cavity QED: strong coupling in organic thin films. *Org. Electron.* 8:94–113
20. Kéna-Cohen S, Forrest SR. 2010. Room-temperature polariton lasing in an organic single-crystal microcavity. *Nat. Photonics* 4:371–75
21. Kéna-Cohen S, Davanço M, Forrest S. 2008. Strong exciton-photon coupling in an organic single crystal microcavity. *Phys. Rev. Lett.* 101:116401
22. Daskalakis KS, Maier SA, Murray R, Kéna-Cohen S. 2014. Nonlinear interactions in an organic polariton condensate. *Nat. Mater.* 13:271–78
23. Daskalakis KS, Maier SA, Kéna-Cohen S. 2015. Spatial coherence and stability in a disordered organic polariton condensate. *Phys. Rev. Lett.* 115:035301
24. Grant RT, Michetti P, Musser AJ, Gregoire P, Virgili T, et al. 2016. Efficient radiative pumping of polaritons in a strongly coupled microcavity by a fluorescent molecular dye. *Adv. Opt. Mater.* 4:1615–23
25. Cookson T, Georgiou K, Zasedatelev A, Grant RT, Virgili T, et al. 2017. A yellow polariton condensate in a dye filled microcavity. *Adv. Opt. Mater.* 5:1700203
26. Rajendran SK, Wei M, Ohadi H, Ruseckas A, Turnbull GA, Samuel IDW. 2019. Low threshold polariton lasing from a solution-processed organic semiconductor in a planar microcavity. *Adv. Opt. Mater.* 7:1801791
27. Yagafarov T, Sannikov D, Zasedatelev A, Georgiou K, Baranikov A, et al. 2020. Mechanisms of blueshifts in organic polariton condensates. *Commun. Phys.* 3:18
28. Plumhof JD, Stöferle T, Mai L, Scherf U, Mahr RF. 2014. Room-temperature Bose–Einstein condensation of cavity exciton–polaritons in a polymer. *Nat. Mater.* 13:247–52
29. Scafirimuto F, Urbonas D, Scherf U, Mahr RF, Stöferle T. 2018. Room-temperature exciton-polariton condensation in a tunable zero-dimensional microcavity. *ACS Photonics* 5:85–89
30. Wei M, Rajendran SK, Ohadi H, Tropf L, Gather MC, et al. 2019. Low threshold polariton lasing in a highly disordered conjugated polymer. *Optica* 6:1124–49
31. Dietrich CP, Steude A, Tropf L, Schubert M, Kronenberg NM, et al. 2016. An exciton-polariton laser based on biologically produced fluorescent protein. *Sci. Adv.* 2:e1600666
32. Betzold S, Dusel M, Kyriienko O, Dietrich CP, Klempt S, et al. 2020. Coherence and interaction in confined room-temperature polariton condensates with Frenkel excitons. *ACS Photonics* 7:384–92
33. Sun Y, Wen P, Yoon Y, Liu G, Steger M, et al. 2017. Bose-Einstein condensation of long-lifetime polaritons in thermal equilibrium. *Phys. Rev. Lett.* 118:016602
34. Pope M, Swenberg C. 1999. *Electronic Processes in Organic Crystals and Polymers*. Oxford, UK: Oxford Univ. Press
35. Agranovich VM. 2008. Hybrid organic-inorganic nanostructures and light-matter interaction. In *Problems of Condensed Matter Physics*, ed. AL Ivanov, SG Tikhodeev, pp. 24–42. Oxford, UK: Oxford Univ. Press
36. Barford W. 2013. *Electronic and Optical Properties of Conjugated Polymers*. Oxford, UK: Oxford Univ. Press
37. Savona V, Andreani L, Schwendimann P, Quattropani A. 1995. Quantum well excitons in semiconductor microcavities: unified treatment of weak and strong coupling regimes. *Solid State Commun.* 93:733–39

38. Chikkaraddy R, de Nijs B, Benz F, Barrow SJ, Scherman OA, et al. 2016. Single-molecule strong coupling at room temperature in plasmonic nanocavities. *Nature* 535:127–30
39. Kéna-Cohen S, Maier SA, Bradley DDC. 2013. Ultrastrongly coupled exciton-polaritons in metal-clad organic semiconductor microcavities. *Adv. Opt. Mater.* 1:827–33
40. Panzarini G, Andreani LC, Armitage A, Baxter D, Skolnick MS, et al. 1999. Exciton-light coupling in single and coupled semiconductor microcavities: polariton dispersion and polarization splitting. *Phys. Rev. B* 59:5082–89
41. Besga B, Vanepf C, Reichel J, Estève J, Reinhard A, et al. 2015. Polariton boxes in a tunable fiber cavity. *Phys. Rev. Appl.* 3:014008
42. Ramezani M, Halpin A, Fernández-Domínguez AI, Feist J, Rodriguez SRK, et al. 2017. Plasmon-exciton-polariton lasing. *Optica* 4:31–37
43. Hakala TK, Moilanen AJ, Vkevinen AI, Guo R, Martikainen JP, et al. 2018. Bose–Einstein condensation in a plasmonic lattice. *Nat. Phys.* 14:739–44
44. Ballarini D, De Giorgi M, Gambino S, Lerario G, Mazzeo M, et al. 2014. Polariton-induced enhanced emission from an organic dye under the strong coupling regime. *Adv. Opt. Mater.* 2:1076–81
45. Haken H. 1970. The semiclassical and quantum theory of the laser. In *Quantum Optics*, ed. SM Kay, A Maitland, pp. 201–321. New York: Academic
46. Staliunas K, Sanchez-Morcillo VJ. 2003. *Transverse Patterns in Nonlinear Optical Resonators*. Berlin: Springer-Verlag
47. Aranson I, Kramer L. 2002. The world of the complex Ginzburg-Landau equation. *Rev. Mod. Phys.* 74:99–143
48. Ciuti C, Savona V, Piermarocchi C, Quattropani A, Schwendimann P. 1998. Threshold behaviour in the collision broadening of microcavity polaritons. *Phys. Rev. B* 58:R10123
49. Wouters M, Carusotto I. 2007. Excitations in a nonequilibrium Bose-Einstein condensate of exciton polaritons. *Phys. Rev. Lett.* 99:140402
50. Bobrovska N, Matuszewski M, Daskalakis KS, Maier SA, Kéna-Cohen S. 2017. Dynamical instability of a nonequilibrium exciton-polariton condensate. *ACS Photonics* 5:111–18
51. Baboux F, De Bernardis D, Goblot V, Gladilin V, Gomez C, et al. 2018. Unstable and stable regimes of polariton condensation. *Optica* 5:1163–70
52. Bajoni D, Senellart P, Lemaître A, Bloch J. 2007. Photon lasing in GaAs microcavity: similarities with a polariton condensate. *Phys. Rev. B* 76:201305
53. Rubo YG, Kavokin AV, Shelykh IA. 2006. Suppression of superfluidity of exciton-polaritons by magnetic field. *Phys. Lett. A* 358:227–30
54. Larionov A, Kulakovskii V, Höfling S, Schneider C, Worschech L, Forchel A. 2010. Polarized nonequilibrium Bose-Einstein condensates of spinor exciton polaritons in a magnetic field. *Phys. Rev. Lett.* 105:256401
55. Rahimi-Iman A, Schneider C, Fischer J, Holzinger S, Amthor M, et al. 2011. Zeeman splitting and diamagnetic shift of spatially confined quantum-well exciton polaritons in an external magnetic field. *Phys. Rev. B* 84:165325
56. Assmann M, Tempel JS, Veit F, Bayer M, Rahimi-Iman A, et al. 2011. From polariton condensates to highly photonic quantum degenerate states of bosonic matter. *PNAS* 108:1804–9
57. Tempel JS, Veit F, Aßmann M, Kreilkamp LE, Rahimi-Iman A, et al. 2012. Characterization of two-threshold behavior of the emission from a GaAs microcavity. *Phys. Rev. B* 85:075318
58. Kammann E, Ohadi H, Maragkou M, Kavokin AV, Lagoudakis PG. 2012. Crossover from photon to exciton-polariton lasing. *New J. Phys.* 14:105003
59. Yamaguchi M, Kamide K, Nii R, Ogawa T, Yamamoto Y. 2013. Second thresholds in BEC-BCS-laser crossover of exciton-polariton systems. *Phys. Rev. Lett.* 111:026404
60. Hanai R, Edelman A, Ohashi Y, Littlewood PB. 2019. Non-Hermitian phase transition from a polariton Bose-Einstein condensate to a photon laser. *Phys. Rev. Lett.* 122:185301
61. Malpuech G, Rubo YG, Laussy FP, Bigenwald P, Kavokin AV. 2003. Polariton laser: thermodynamics and quantum kinetic theory. *Semicond. Sci. Technol.* 18:S395–404
62. Cao HT, Doan TD, Tran Thoai DB, Haug H. 2004. Condensation kinetics of cavity polaritons interacting with a thermal phonon bath. *Phys. Rev. B* 69:245325

63. Doan TD, Cao HT, Tran Thoai DB, Haug H, Thoai D, Haug H. 2005. Condensation kinetics of microcavity polaritons with scattering by phonons and polaritons. *Phys. Rev. B* 72:085301
64. Deng H, Haug H, Yamamoto Y. 2010. Exciton-polariton Bose-Einstein condensation. *Rev. Mod. Phys.* 82:1489
65. Mazza L, La Rocca GC. 2009. Organic-based microcavities with vibronic progressions: photoluminescence. *Phys. Rev. B* 80:235314
66. Kasprzak J, André R, Dang L, Shelykh I, Kavokin A, et al. 2007. Build up and pinning of linear polarization in the Bose condensates of exciton polaritons. *Phys. Rev. B* 75:045326
67. Manni F, Lagoudakis KG, Liew TCH, André R, Deveaud-Plédran B. 2011. Spontaneous pattern formation in a polariton condensate. *Phys. Rev. Lett.* 107:106401
68. Slootsky M, Zhang Y, Forrest SR. 2012. Temperature dependence of polariton lasing in a crystalline anthracene microcavity. *Phys. Rev. B* 86:045312
69. Mizuno H, Akagi H, Tsubouchi M, Itakura R, Katsuki H, Yanagi H. 2019. Incident angle and photon energy dependence of polariton lasing in an organic microcavity. *Jpn. J. Appl. Phys.* 58:052003
70. Sannikov D, Yagafarov T, Georgiou K, Zasedatelev A, Baranikov A, et al. 2019. Room temperature broadband polariton lasing from a dye-filled microcavity. *Adv. Opt. Mater.* 7:1900163
71. Oulton RF, Takada N, Koe J, Stavrinou PN, Bradley DDC. 2003. Strong coupling in organic semiconductor microcavities. *Semicond. Sci. Technol.* 18:S419–27
72. Holmes RJ, Forrest SR. 2005. Exciton-photon coupling in organic materials with large intersystem crossing rates and strong excited-state molecular relaxation. *Phys. Rev. B* 71:235203
73. Agranovich VM, Litinskaia M, Lidzey DG. 2003. Cavity polaritons in microcavities containing disordered organic semiconductors. *Phys. Rev. B* 67:085311
74. Kéna-Cohen S, Forrest S. 2008. Giant Davydov splitting of the lower polariton branch in a polycrystalline tetracene microcavity. *Phys. Rev. B* 77:073205
75. Litinskaya M, Reineker P, Agranovich VM. 2004. Exciton-polaritons in a crystalline anisotropic organic microcavity. *Phys. Status Solidi* 201:646–54
76. Kondo H, Yamamoto Y, Takeda A, Yamamoto S, Kurisu H. 2008. Optical responses in single-crystalline organic microcavities. *J. Lumin.* 128:777–79
77. Tsuchimoto Y, Nagai H, Amano M, Bando K, Kondo H. 2014. Cavity polaritons in an organic single-crystalline rubrene microcavity. *Appl. Phys. Lett.* 104:233307
78. Davydov A. 1971. *Theory of Molecular Excitons*. New York: Springer
79. Philpott MR. 1971. Calculation of the exciton band structure of the 3800- and 2500-Å singlet transitions of crystalline anthracene. *J. Chem. Phys.* 54:111–13
80. Kéna-Cohen S, Davanço M, Forrest SR. 2008. Resonant Rayleigh scattering from an anisotropic organic single-crystal microcavity. *Phys. Rev. B* 78:153102
81. Mazza L, Kéna-Cohen S, Michetti P, La Rocca GC. 2013. Microscopic theory of polariton lasing via vibronically assisted scattering. *Phys. Rev. B* 88:075321
82. Forrest SR. 2004. The path to ubiquitous and low-cost organic electronic appliances on plastic. *Nature* 428:911–18
83. Yokoyama D, Sakaguchi A, Suzuki M, Adachi C. 2008. Horizontal molecular orientation in vacuum-deposited organic amorphous films of hole and electron transport materials. *Appl. Phys. Lett.* 93:173302
84. Wu CC, Lin YT, Wong KT, Chen RT, Chien YY. 2004. Efficient organic blue-light-emitting devices with double confinement on terfluorenes with ambipolar carrier transport properties. *Adv. Mater.* 16:61–65
85. Lin HW, Lin CL, Chang HH, Lin YT, Wu CC, et al. 2004. Anisotropic optical properties and molecular orientation in vacuum-deposited ter(9,9-diarylfluorene)s thin films using spectroscopic ellipsometry. *J. Appl. Phys.* 95:881–86
86. Lerario G, Fieramosca A, Barachati F, Ballarini D, Daskalakis KS, et al. 2017. Room-temperature superfluidity in a polariton condensate. *Nat. Phys.* 13:837–41
87. Müller JG, Lemmer U, Raschke G, Anni M, Scherf U, et al. 2003. Linewidth-limited energy transfer in single conjugated polymer molecules. *Phys. Rev. Lett.* 91:267403

88. Hertel D, Bassler H, Scherf U, Horhold HH. 1999. Charge carrier transport in conjugated polymers. *J. Chem. Phys.* 110:9214–22
89. Stampfl J, Tasch S, Leising G, Scherf U. 1995. Quantum efficiencies of electroluminescent poly(paraphenylenes). *Synth. Met.* 71:2125–28
90. Laquai F, Mishra AK, Müllen K, Friend RH. 2008. Amplified spontaneous emission of poly(ladder-type phenylene)s—the influence of photophysical properties on ASE thresholds. *Adv. Funct. Mater.* 18:3265–75
91. Cubitt AB, Heim R, Adams SR, Boyd AE, Gross LA, Tsien RY. 1995. Understanding, improving and using green fluorescent proteins. *Trends Biochem. Sci.* 20:448–55
92. Agranovich V, Tshich B. 1968. Collective properties of Frenkel excitons. *Sov. Phys. JETP* 26:104–12
93. Combescot M, Pogosov W. 2009. Composite boson many-body theory for Frenkel excitons. *Eur. Phys. J. B* 68:161–81
94. Eastham P, Littlewood P. 2000. Bose condensation in a model microcavity. *Solid State Commun.* 116:357–61
95. Galego J, Garcia-Vidal FJ, Feist J. 2015. Cavity-induced modifications of molecular structure in the strong-coupling regime. *Phys. Rev. X* 5:41022
96. Flick J, Appel H, Ruggenthaler M, Rubio A. 2017. Cavity Born–Oppenheimer approximation for correlated electron–nuclear–photon systems. *J. Chem. Theory Comput.* 13:1616–25
97. Ćwik JA, Reja S, Littlewood PB, Keeling J. 2014. Polariton condensation with saturable molecules dressed by vibrational modes. *Europhys. Lett.* 105:47009
98. Martínez-Martínez LA, Eizner E, Kéna-Cohen S, Yuen-Zhou J. 2019. Triplet harvesting in the polaritonic regime: a variational polaron approach. *J. Chem. Phys.* 151:054106
99. Breuer HP, Petruccione F. 2002. *The Theory of Open Quantum Systems*. Oxford, UK: Oxford Univ. Press
100. Strashko A, Kirton P, Keeling J. 2018. Organic polariton lasing and the weak to strong coupling crossover. *Phys. Rev. Lett.* 121:193601
101. Baldo MA, Holmes RJ, Forrest SR. 2002. Prospects for electrically pumped organic lasers. *Phys. Rev. B* 66:035321
102. Yang Y, Turnbull GA, Samuel IDW. 2008. Hybrid optoelectronics: a polymer laser pumped by a nitride light-emitting diode. *Appl. Phys. Lett.* 92:163306
103. Holmes RJ, Kéna-Cohen S, Menon VM, Forrest SR. 2006. Strong coupling and hybridization of Frenkel and Wannier–Mott excitons in an organic–inorganic optical microcavity. *Phys. Rev. B* 74:235211
104. Paschos GG, Somaschi N, Tsintzos SI, Coles D, Bricks JL, et al. 2017. Hybrid organic–inorganic polariton laser. *Sci. Rep.* 7:11377
105. Agranovich VM, Gartstein YN, Litinskaya M. 2011. Hybrid resonant organic–inorganic nanostructures for optoelectronic applications. *Chem. Rev.* 111:5179–214
106. Herrera F, Spano FC. 2017. Dark vibronic polaritons and the spectroscopy of organic microcavities. *Phys. Rev. Lett.* 118:223601
107. Herrera F, Spano FC. 2016. Cavity-controlled chemistry in molecular ensembles. *Phys. Rev. Lett.* 116:238301
108. Orgiu E, George J, Hutchison JA, Devaux E, Dayen JF, et al. 2015. Conductivity in organic semiconductors hybridized with the vacuum field. *Nat. Mater.* 14:1123–29
109. Stranius K, Hertzog M, Brjesson K. 2018. Selective manipulation of electronically excited states through strong light–matter interactions. *Nat. Commun.* 9:2273
110. Eizner E, Martínez-Martínez LA, Yuen-Zhou J, Kéna-Cohen S. 2019. Inverting singlet and triplet excited states using strong light–matter coupling. *Sci. Adv.* 5:eaax4482